Chinese Chemical Letters 37 (2026) 111348

Contents lists available at ScienceDirect

Chinese Chemical Letters

journal homepage: www.elsevier.com/locate/cclet

Mesoporous carbon anchored with zincophilic nitrogen and oxygen sites as protective layer for enhanced stability of Zn anodes

Zhuohua Li[a], Qizhen Zhu[a,*], Yanze Li[a], Yong Yang[a], Yuan Ju[a], Mengyao Xu[a], Bin Xu[a,b,*]

[a] State Key Laboratory of Organic-Inorganic Composites, Beijing Key Laboratory of Electrochemical Process and Technology for Materials, Beijing University of Chemical Technology, Beijing 100029, China
[b] Shaanxi Key Laboratory of Chemical Reaction Engineering, School of Chemistry and Chemical Engineering, Yan'an University, Yan'an 716000, China

ARTICLE INFO

Article history:
Received 16 April 2025
Revised 14 May 2025
Accepted 19 May 2025
Available online 19 May 2025

Keywords:
Mesoporous carbon
Nitrogen and oxygen sites
Protective layer
Zn anodes
Aqueous zinc-ion batteries

ABSTRACT

Aqueous zinc-ion batteries are promising candidates for large-scale energy storage, but their practical application is hindered by the issues of Zn dendrite growth and side reactions. To address these challenges, a mesoporous carbon anchored with zincophilic nitrogen and oxygen sites (NOPC) is prepared by pyrolyzing NH_4Cl-incorporated ZIF-8 and constructed as a protective layer on Zn anode. In the NOPC layer, the zincophilic nitrogen and oxygen sites facilitate uniform Zn^{2+} nucleation, while the abundant mesopores homogenize Zn^{2+} flux, effectively enabling dendrite-free deposition. Moreover, the NOPC layer suppresses interfacial side reactions by isolating the Zn surface from active H_2O. Remarkably, the Zn anode protected by the NOPC layer achieves an ultralong cycle life exceeding 6000 h at 1 mA/cm^2 and 1 mAh/cm^2, and maintains a high Coulombic efficiency of 99.8 % for 4600 cycles, indicating superior stability and reversibility. When paired with $NaV_3O_8{\cdot}1{\cdot}5H_2O$ cathode, the full cell displays a capacity retention of 85.1 % after 3000 cycles at 5 A/g. This study demonstrates that the engineering of zincophilic sites and meso–porosity in carbon-based protective layers represents an effective strategy for enhancing the performance of aqueous zinc-ion batteries.

© 2026 Published by Elsevier B.V. on behalf of Chinese Chemical Society and Institute of Materia Medica, Chinese Academy of Medical Sciences.

Aqueous zinc-ion batteries (AZIBs) have emerged as a promising candidate for large-scale energy storage, as the Zn anode offers a high theoretical capacity of 820 mAh/g, a suitable redox potential and abundant resource availability [1]. However, their commercial application is hindered by critical challenges in terms of cycle stability and reversibility. During plating/stripping cycles, the Zn anode is highly susceptible to the formation and growth of zinc dendrites, leading to a severe risk of internal short circuits [2,3]. Moreover, the thermodynamic instability of Zn metal in aqueous environments readily triggers side reactions, including hydrogen evolution (HER), corrosion, and passivation, which compromise Coulombic efficiency (CE) and accelerate capacity degradation [4,5].

To address these issues, various strategies have been explored, including electrolyte optimization [6,7], three-dimensional Zn anode structural design [8,9], and protective interface engineering [10–12]. Among these approaches, the construction of protective layers on the Zn anode surface stands out due to its simplicity and effectiveness. Various materials, including carbon-based substances [13,14], metal alloys [15,16], metal oxides [17,18], and polymers [19,20], have been employed as protective layer materials. Carbon materials, especially, have garnered significant attention for Zn anode modification. Owing to their excellent electronic conductivity, chemical stability and diverse structural tunability, carbon-based protective layers can enable uniform electric field distribution at the Zn anode/electrolyte interface and facilitate fast Zn^{2+} transport [21–23]. For instance, Li *et al.* [24] coated the activated carbon onto the zinc foil as a protective layer, utilizing its large specific surface area to provide numerous active sites for homogeneous Zn^{2+} deposition, thereby extending the cycle life of the Zn anode from several tens of hours to 250 h. However, carbon protective layers still face challenges in fully suppressing dendrite formation under high Zn deposition capacities or prolonged plating/stripping cycles due to their inherently low affinity for zinc.

Anchoring highly zincophilic heteroatoms, such as nitrogen and oxygen, into carbon-based protective layers is an efficient strategy for creating uniformly distributed Zn^{2+} nucleation sites, which can improve the uniformity of Zn^{2+} deposition [25,26]. For example, Zhou *et al.* [27] developed a N-doped graphene layer on the Zn anode surface, where the nitrogen sites significantly increased zincophilicity and the Zn^{2+} nucleation site density, effectively extending the cycle life of the Zn anode to 1200 h. Beyond surface

* Corresponding authors.
E-mail addresses: zhuqz@mail.buct.edu.cn (Q. Zhu), xubin@mail.buct.edu.cn (B. Xu).

https://doi.org/10.1016/j.cclet.2025.111348
1001-8417/© 2026 Published by Elsevier B.V. on behalf of Chinese Chemical Society and Institute of Materia Medica, Chinese Academy of Medical Sciences.

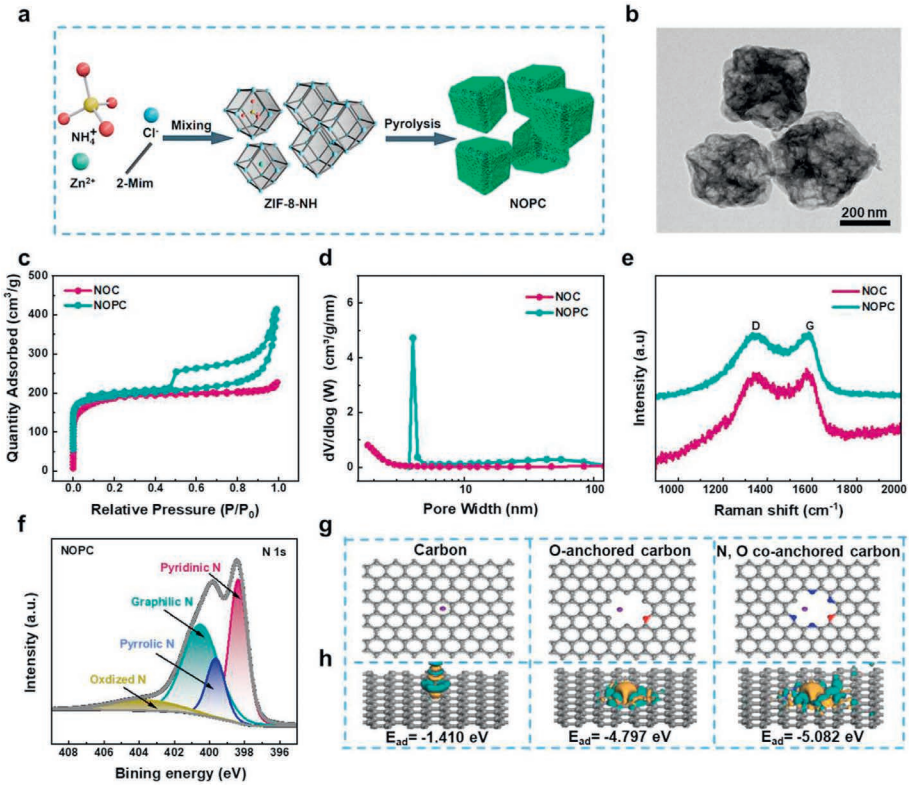


Fig. 1. (a) Schematic of preparation process, (b) TEM image, (c) N_2 (77 K) adsorption-desorption isotherms, (d) pore size distribution, (e) Raman pattern, and (f) N 1s XPS spectrum of NOPC. (g) Theoretical simulations of the adsorption of Zn on carbon, O-anchored carbon and N,O co-anchored carbon with (h) the corresponding adsorption energies and electron density differences.

chemistry, the porous structure of carbon-based materials can considerably homogenize interfacial Zn^{2+} flux and improve Zn^{2+} deposition kinetics, further enhancing the stability of the Zn anode [28–30]. Therefore, the development of carbon-based protective layer materials that feature abundant zincophilic sites for effective Zn^{2+} nucleation and advanced meso–porosity for rapid Zn^{2+} transport is crucial for achieving dendrite-free Zn anodes. Here, we propose a mesoporous carbon material, anchored with massive nitrogen and oxygen heteroatoms (NOPC), as an artificial protective layer on the surface of the Zn anode, in which the plentiful N and O sites facilitate uniform Zn^{2+} nucleation, while the abundant mesopores serve to homogenize the Zn^{2+} flux and accelerate deposition kinetics, thereby efficiently protecting the Zn anode from dendrite growth and interfacial instability.

The NOPC material was designed and prepared using ZIF-8 MOF as a precursor, along with NH_4Cl-derived etching (Fig. 1a). The ZIF-8 MOF with NH_4Cl incorporated in its backbone (ZIF-8-NH) was prepared by stirring a mixture of $Zn(CH_3COO)_2$, NH_4Cl, 2MI, and CTAB. During the subsequent pyrolysis, massive N and O heteroatoms from the ZIF-8 ligands were retained within the carbon matrix. Concurrently, the decomposition products of NH_4Cl etched the MOF-derived carbon framework, constructing a well-developed mesoporous structure. For comparison, a less porous carbon material (NOC) was synthesized from ZIF-8 without the addition of NH_4Cl.

The TEM image in Fig. 1b reveals that the NOPC particles, uniform in size (~200 nm), retain the rhombohedral polyhedral morphology of the ZIF-8-NH (Fig. S1 in Supporting information) and display a mesoporous structure. In contrast, the NOC material shows similar particle size but lacks meso–porosity (Fig. S2 in Supporting information). The XRD pattern of ZIF-8-NH shows the same crystal structure as ZIF-8, while the NOPC exhibits diffraction peaks at 24.06° and 43.58°, corresponding to the graphitic carbon (Fig. S3 in Supporting information) [31]. These results suggest that the NH_4Cl in the ZIF-8 backbone primarily etches the internal carbon structure during pyrolysis without altering its crystalline features or external morphology. Moreover, N_2 (77 K) adsorption-desorption isotherms were employed to analyze the structural characteristics of NOPC and NOC (Figs. 1c and d). The NOC sample exhibits type I isotherms, characteristic of a microporous structure with pore size below 2 nm. By contrast, NOPC displays type IV isotherm with a pronounced hysteresis loop at high relative pressures, confirming the presence of abundant mesopores. Additionally, NOPC features a high pore volume of 0.68 cm^3/g and a large specific surface area of 587 m^2/g, with pore sizes centered at ~5 nm, highlighting its potential for facilitating rapid ion transport.

The Raman spectra of NOPC and NOC (Fig. 1e) reveal the disorder carbon D peak (1360 cm^{-1}) and the graphitic carbon G peak (1580 cm^{-1}) [32]. The I_D/I_G ratio, calculated from the peak areas, is 3.16 for NOPC, higher than that of NOC (2.96), indicating a lower graphitization degree due to the additional defects caused by NH_4Cl-derived etching. Besides, the FTIR spectra of NOPC and NOC (Fig. S4 in Supporting information) present similar peaks related to the stretching vibrations of the -OH (3417 cm^{-1}), C=O (1660 cm^{-1}), C=N (1573 cm^{-1}), and C–O (1232 cm^{-1}) groups, which significantly promote ion transport and facilitate even Zn^{2+} deposition [33]. The EDS mappings of NOPC (Fig. S5 in Supporting information) demonstrate the uniform distribution of O, N, and C elements, and the XPS spectrum (Fig. S6 in Supporting information) further quantifies the N (8.27 at%) and O (11.91 at%) contents, verifying the anchoring of these zincophilic sites. The N 1s peaks in Fig. 1f identify the presence of pyridine N, pyrrole N, graphitic N, and oxidized N. The pyridine N and pyrrole N induce external defects and promote increased Zn^{2+} flux, while the graphitic N enhances the electronic conductivity of the carbon matrix [34]. The O 1s spectrum (Fig. S7 in Supporting information) shows the peaks corresponding to C=O

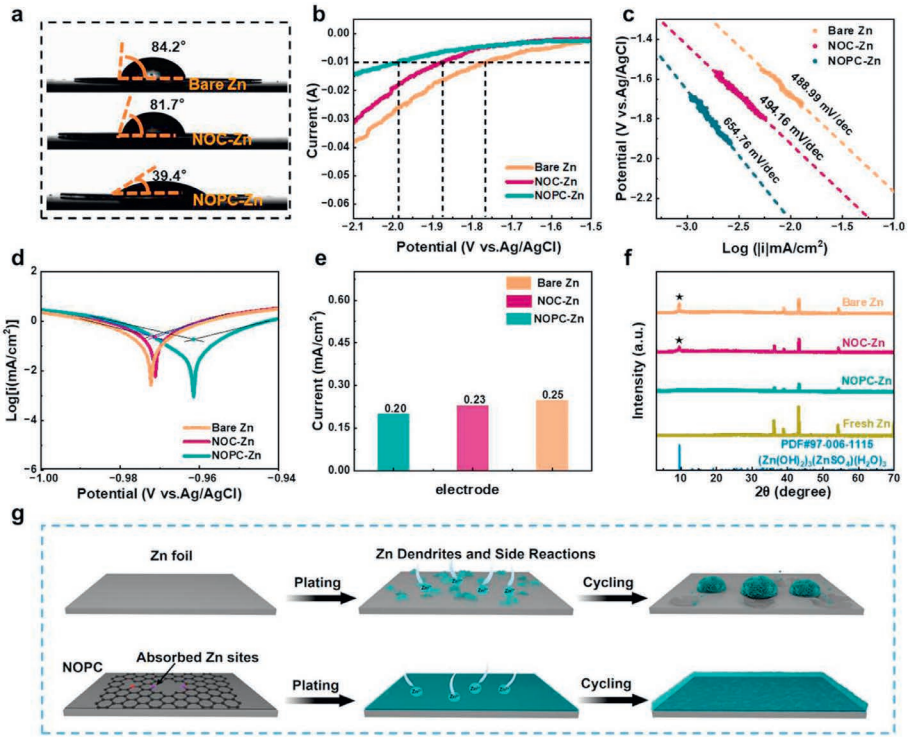


Fig. 2. (a) Contact angles with the electrolyte, (b) LSV curves, (c) Tafel slopes, (d) linear polarization curves, and (e) corrosion currents, of bare Zn, NOC-Zn, and NOPC-Zn. (f) XRD patterns of the electrodes after immersion in the electrolyte for 12 days. (g) Schematics of the Zn deposition on bare Zn and NOPC-Zn surface.

and C–O groups, which can improve the wettability of the NOPC-Zn/electrolyte interface.

DFT calculations reveal the superiority of NOPC in guiding Zn adsorption as a protective layer (Fig. 1g). The adsorption energy of Zn on pristine carbon layer is −1.410 eV. Upon anchoring O atoms, the Zn adsorption energy strengthens to −4.797 eV. Further anchoring both N and O atoms create additional defects and further enhances the Zn adsorption energy to −5.082 eV. The electron density differences (Fig. 1h) confirms strong Zn binding at the nitrogen sites and defect regions in the N, O co-anchored carbon. Therefore, the NOPC material with N, O co-anchoring and developed mesoporous structure can synergistically improve Zn^{2+} transport, nucleation, and uniform deposition, promising highly stable Zn electrode.

Due to its oxygen-containing groups and abundant mesopores, the NOPC protective layer significantly enhances the wettability of the Zn electrode with the electrolyte, resulting in a small contact angle of 39.4° (Fig. 2a), which is beneficial for promoting high Zn^{2+} flux at the interface. Meanwhile, the NOPC layer serves as a barrier against side reactions triggered by active H_2O molecules, such as HER, corrosion, and passivation. The linear sweep voltammetry (LSV) curves in Fig. 2b demonstrate superior HER suppression for NOPC-Zn with the HER potential of −1.98 V (*vs.* Ag/AgCl) at 10 mA, compared to NOC-Zn (−1.87 V *vs.* Ag/AgCl) and bare Zn (−1.77 V *vs.* Ag/AgCl). The higher Tafel slope (654.76 mV/dec) in Fig. 2c further indicates its enhanced resistance to HER. Linear polarization measurements (Figs. 2d and e) reveal that NOPC-Zn displays improved corrosion resistance characterized by a higher corrosion potential of −0.961 V (*vs.* Ag/AgCl) and a notably lower corrosion current of 0.20 mA/cm^2, compared to NOC-Zn and bare Zn. As shown in Fig. 2f, the XRD pattern of the NOPC-Zn electrode, immersed in 2 mol/L $ZnSO_4$ electrolyte for 12 days, shows no characteristic peak of $Zn_4SO_4(OH)_6{\cdot}3H_2O$ by-products, confirming that the NOPC layer effectively inhibits the passivation of the Zn electrode.

Based on the above analysis, the Zn^{2+} deposition behavior on the Zn electrodes with and without the NOPC protective layer is illustrated in Fig. 2g. The bare Zn electrode, with a limited number of nucleation sites, suffers from the formation of extensive zinc dendrites and the serious side reactions. In contrast, the NOPC layer on the Zn electrode, enriched with nitrogen and oxygen atoms, provides abundant nucleation sites and exhibits developed meso–porosity, enabling high Zn^{2+} flux and homogenous electric field distribution. The NOPC layer also acts as a barrier against the active H_2O, significantly suppressing the interfacial side reactions, thereby facilitating uniform Zn^{2+} deposition and enhancing the stability of the Zn electrode.

To validate the role of the NOPC protective layer in promoting uniform Zn deposition, symmetric cells with NOPC-Zn and bare Zn electrodes were assembled to investigate the morphological evolutions of these electrodes during Zn^{2+} deposition. *In situ* optical microscopy visualizations reveal that at a current density of 10 mA/cm^2, bare Zn exhibits disordered Zn dendrites within 30 min (Fig. 3a), while the NOPC-Zn electrode maintains a smooth and uniform surface (Fig. 3b). The deposition morphologies of the Zn electrodes were further characterized by SEM and AFM. With a plating capacity of 5 mAh/cm^2, the bare Zn electrode displays numerous Zn flakes that are irregularly stacked upright on the surface (Fig. 3c), which evolve into disordered Zn dendrites as the capacity increases to 10 mAh/cm^2 (Fig. 3d). However, the NOC-Zn electrode displays negligible Zn flakes (Fig. S8 in Supporting information), while the NOPC-Zn maintains smooth surface without Zn flakes even with 10 mAh/cm^2 (Figs. 3e and f), confirming the effectiveness of the NOPC layer in homogenizing Zn^{2+} deposition. AFM images show significant height fluctuations on bare Zn with the capacity increasing from 5 mAh/cm^2 to 10 mAh/cm^2 (Fig. 3g and Fig. S9 in Supporting information). In contrast, the NOPC-Zn electrode exhibits smooth morphology with minimal height fluctuations even at 10 mAh/cm^2 (Fig. 3h and Fig. S10 in Supporting information). Furthermore, quantitative roughness data (Fig. 3i and Fig. S11 in Supporting information) reveal a sharp increase in surface roughness of 100 nm on bare Zn from 5 mAh/cm^2 to 10 mAh/cm^2 due to the dendritic accumulation. Conversely, the

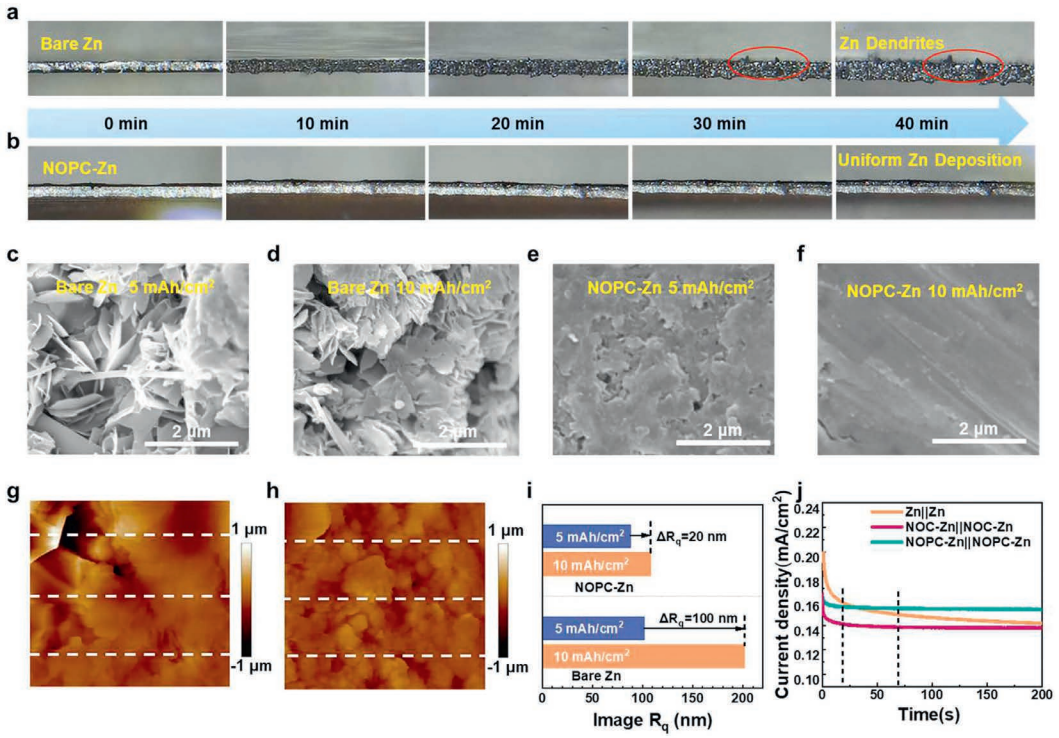


Fig. 3. *In situ* optical microscopy of (a) bare Zn and (b) NOPC-Zn during Zn^{2+} plating. SEM images of (c, d) bare Zn and (e, f) NOPC-Zn with different Zn plating capacities. AFM images of (g) bare Zn and (h) NOPC-Zn with a plating capacity of 10 mAh/cm^2. (i) Average height of bare Zn and NOPC-Zn after Zn plating. (j) CA curves of symmetric cells with bare Zn, NOC-Zn, and NOPC-Zn.

NOPC-Zn electrode exhibits only a slight increase of 20 nm in surface roughness, reflecting its compact and uniform deposition morphology enabled by the NOPC protective layer that guides homogeneous Zn^{2+} deposition and suppress the dendrite growth.

Chronoamperometry (CA) tests were conducted to study the Zn^{2+} migration, nucleation and deposition behaviors on the electrodes. As depicted in Fig. 3j, at an overpotential of 10 mV, the bare Zn electrode exhibits continuously declining current density for over 200 s, indicating uncontrollable two-dimensional (2D) diffusion of Zn^{2+} on the surface, leading to uneven, dendrite growth, and eventually accelerated electrode failure. In contrast, the NOC-Zn electrode requires 65 s to complete 2D diffusion, while the NOPC-Zn electrode achieves current equilibrium for three-dimensional Zn^{2+} diffusion within 20 s. This improvement is ascribed to the NOPC layer, which is rich in zincophilic N and O atoms as nucleation sites and offers numerous mesopores that promote efficient Zn^{2+} diffusion, thereby effectively suppressing the Zn dendrite formation and improving the electrode stability.

The stability and reversibility of the Zn electrodes with and without the protective layers were evaluated through electrochemical plating/stripping analyses using symmetric cells with NOPC-Zn, NOC-Zn, and bare Zn electrodes. As revealed in the EIS spectra in Fig. 4a, the charge transfer resistance (R_{ct}) of NOPC-Zn is 495 Ω, significantly lower than that of bare Zn (1716 Ω) and NOC-Zn (762 Ω). Furthermore, compared to the cells with bare Zn (46 mV) and NOC-Zn (30 mV), the cell with NOPC-Zn shows a much-decreased nucleation overpotential of 22 mV at a current density of 1 mA/cm^2 (Fig. 4b). This improvement is attributed to the N, O co-anchored mesoporous carbon framework of NOPC, which provides abundant zincophilic sites and promote Zn^{2+} flux, leading to fast charge transfer and accelerated nucleation kinetics. As a result, the cell based on the NOPC-Zn electrodes demonstrates the lowest polarization voltage across a range of current densities from 0.5 mA/cm^2 to 10 mA/cm^2 with a capacity of 1 mAh/cm^2 (Fig. 4c). Notably, at a high current density of 10 mA/cm^2, the NOPC-Zn electrode delivers a polarization voltage of 61 mV, much lower than that of bare Zn (121 mV) and NOC-Zn (111 mV), highlighting the role of NOPC layer in boosting the rate capability of Zn electrodes.

The NOPC layer significantly enhances the cycle stability of the Zn electrodes. The bare Zn and NOC-Zn electrodes experience short circuits at 165 h and 445 h, respectively, while the NOPC-Zn in symmetric cell exhibits remarkable stability with an ultra-long cycle life of over 6000 h at 1 mA/cm^2@1 mAh/cm^2 and a low and stable polarization voltage of ~35 mV throughout the cycling process (Fig. 4d and Fig. S12 in Supporting information). The advantages of the NOPC-Zn electrode become even more pronounced as the current density increases (Figs. S13 and S14 in Supporting information). At a current density of 5 mA/cm^2, the bare Zn shows poor cycling stability with a short-circuit after 108 h due to uneven deposition and dendrite formation (Fig. S15a in Supporting information). The NOC-Zn presents a slightly prolonged cycle life of 536 h, which ultimately ends in dendrite-induced failure (Fig. S15b in Supporting information). In contrast, the NOPC-Zn electrode can stably cycle for over 2400 h with a low polarization voltage of ≤90 mV (Fig. 4e, Figs. S15c and d in Supporting information), indicating stable plating/stripping behavior in high-rate cycling. Compared to recently reported carbon-layer-protected Zn electrodes (Table S1 in Supporting information), the NOPC-Zn electrode presented in this work exhibits significantly superior cycling stability with lower electrochemical polarization, effectively validating the efficacy of the NOPC protective layer in suppressing Zn dendrite formation and minimizing side reactions.

The surface morphology of the cycled electrodes confirms the above findings. The bare Zn electrode surface is initially smooth but becomes rough as disordered Zn flakes accumulate on the surface after cycling for 100 h (Fig. S16 in Supporting information). In contrast, the surface of the pristine NOC-Zn and NOPC-Zn electrodes exhibit loose structure (Figs. S17 and S18 in Supporting information), which is favorable for homogenizing the Zn^{2+} flux and exposing the nucleation sites. After repeated Zn plating/stripping

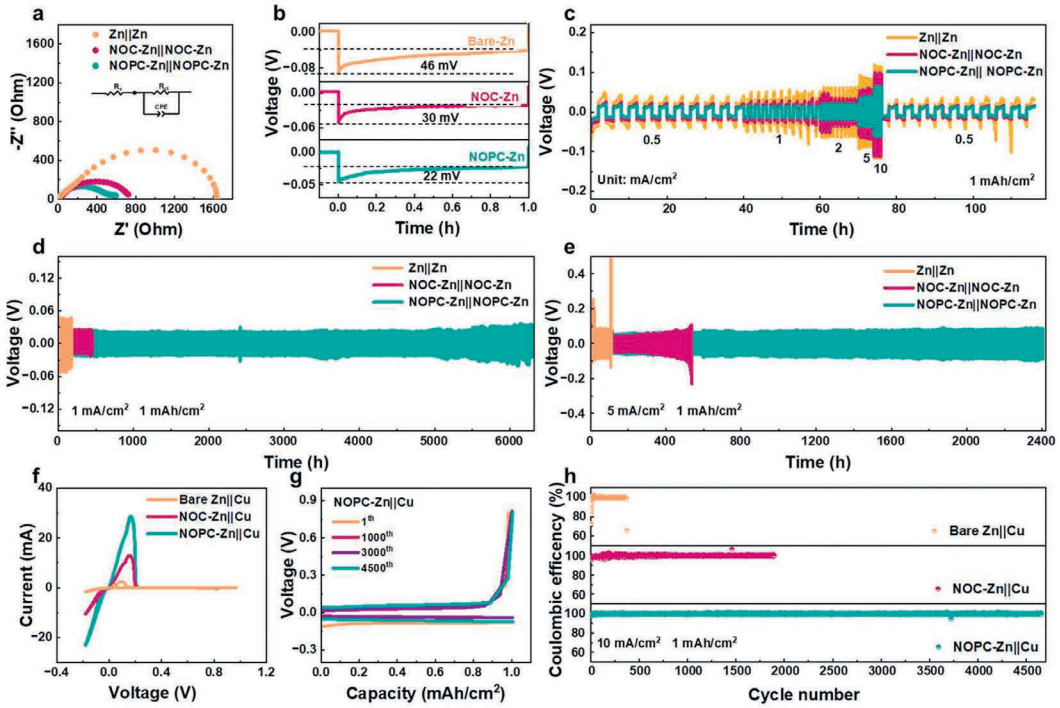


Fig. 4. Performance of symmetric cells based on bare Zn, NOC-Zn, and NOPC-Zn. (a) EIS spectra. (b) Nucleation overpotential at 1 mA/cm^2. (c) Rate performance at 1 mAh/cm^2. Cycling performance at (d) 1 mA/cm^2, 1 mAh/cm^2, and (e) 5 mA/cm^2, 1 mAh/cm^2. Performance of asymmetric cells with bare Zn, NOC-Zn, NOPC-Zn *vs.* Cu: (f) CV curves at 1 mV/s. (g) Charge-discharge profiles of NOPC-Zn||Cu at different cycles. (h) CE profiles at 10 mA/cm^2, 1 mAh/cm^2.

for 100 h, the electrode surfaces become flat and dense without dendrite formation. Remarkably, cross-sectional SEM images verify the uniform, dense, and crack-free deposition in the cycled NOPC-Zn electrode (Fig. S19 in Supporting information). This improvement is attributed to the NOPC protective layer, which prevents uncontrolled Zn dendrite growth, and suppresses undesirable side reactions, thus significantly enhancing the structural stability of the Zn electrode.

The reversibility of Zn^{2+} plating/stripping on the electrodes is evaluated via cyclic voltammetry (CV) curves of asymmetric Zn||Cu cells. Compared to the other two cells, the NOPC-Zn||Cu cell delivers a significantly larger CV enclosed area (Fig. 4f), indicating that the NOPC's N, O co-anchored mesoporous carbon structure provides substantial nucleation sites for reversible Zn^{2+} deposition. The high reversibility of Zn plating/stripping is further corroborated by CE tests. At 5 mA/cm^2, the NOPC-Zn||Cu cell maintains stable CEs of ~99.5 % for over 1800 cycles (Fig. S20 in Supporting information). Notably, when the current density increases to 10 mA/cm^2, the bare Zn||Cu cell fails after 370 cycles with an average CE of only 97.0 % (Figs. 4g and h, Fig. S21 in Supporting information). The NOC-Zn||Cu cell operates for 1800 cycles with an average CE of 99.7 % and a polarization voltage of 158 mV. In contrast, the NOPC-Zn||Cu cell achieves excellent reversibility during ultra-long 4600 cycles, with an average CE of 99.8 % and low polarization (125 mV), revealing the superior reversibility under high current densities.

The NOPC-Zn anode is paired with $NaV_3O_8{\cdot}1{\cdot}5H_2O$ (NVO) cathode to assemble a full cell for evaluating its practical performance (Fig. 5a). The NVO material, prepared by a simple chemical reaction as reported previously [35], exhibits nano-belt structure and XRD peaks corresponding to the *P*21-*m* space group (JCPDS No. 16–0601) (Figs. S22 and S23 in Supporting information). The CV curves of the NOPC-Zn||NVO and bare Zn||NVO full cells at a scan rate of 0.1 mV/s are presented in Fig. 5b and Fig. S24 (Supporting information). Both the cells show two distinct pairs of redox peaks, while the NOPC-Zn||NVO exhibits lower polarization, characterized by narrower anodic/cathodic peak potential gaps (0.198 and 0.184 V *vs.* 0.218 and 0.216 V for bare Zn||NVO). Furthermore, the charging/discharging profiles of the NOPC-Zn||NVO cell at 0.5 mA/g in the initial cycle (Fig. 5c) show a reduced polarization gap of 187 mV between the charging and discharging plateaus, along with a significantly higher capacity (337.3 mAh/g) compared to the bare Zn||NVO cell (237 mV, 204.3 mAh/g), consistent with the CV results.

Based on the enhanced kinetics of the NOPC-Zn anode, the NOPC-Zn||NVO full cell exhibits excellent rate performance. As shown in Fig. 5d, the reversible capacities of the NOPC-Zn||NVO cell at current densities of 0.5, 1, 2, 3, and 5 A/g is 345.5, 321, 306.6, 282.6 and 245.7 mAh/g, respectively, significantly higher than those of the bare Zn||NVO cell. Upon restoring the current density to 0.5 A/g, the reversible capacity of the NOPC-Zn cell reaches 314.5 mAh/g. Additionally, the full cell with the NOPC-Zn anode demonstrates clear characteristic plateaus with a reversible capacity of 245.7 mAh/g at a high current density of 5 A/g (Fig. 5e and Fig. S25 in Supporting information), while the bare Zn||NVO full cell only delivers a capacity of 74.2 mAh/g, confirming the significant contribution of the NOPC layer on the Zn anode in improving the rate performance of AZIBs.

The EIS analysis in Fig. 5f further illustrates the improvement in charge transport kinetics of the NOPC-Zn anode within the full cell configuration. Fitted with the equivalent circuit, the EIS spectrum of the NOPC-Zn||NVO cell reveals a greatly decreased R_{ct} of 48.4 Ω, compared to the bare Zn||NVO cell (240.6 Ω). It indicates that the NOPC layer promotes rapid ion transport and provides massive favorable sites for Zn^{2+} plating/stripping, thereby reducing the interfacial impedance. Consequently, the cell incorporating the NOPC-Zn anode demonstrates much accelerated charge transfer and enhanced Zn plating/stripping kinetics. As a result, the full cell with the NOPC-Zn anode achieves stable cycling for over 3000 cycles with a high capacity retention of 85.1 %, which is signifi-

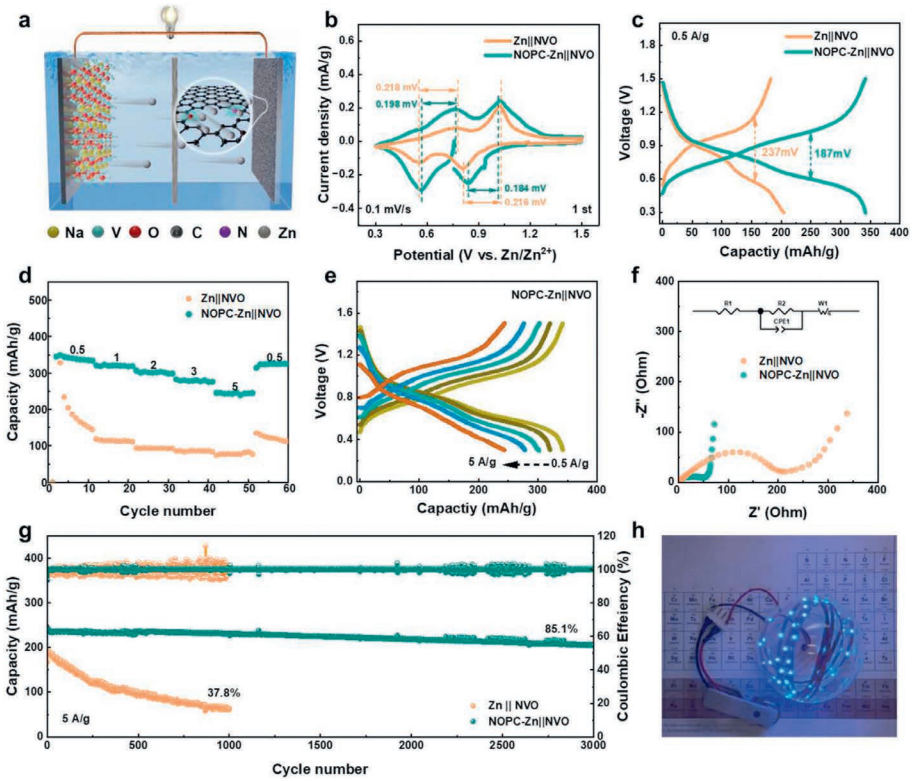


Fig. 5. Electrochemical performance of NOPC-Zn||NVO full cells. (a) Schematic of cell structure. (b) Initial CV curves at 0.1 mV/s. (c) Initial charge-discharge profiles at 0.5 A/g. (d) Rate performance. (e) Charge-discharge profiles at various current densities. (f) EIS spectra with the equivalent circuit in the inset. (g) Long-term cycling performance at 5 A/g. (h) Photograph of NOPC-Zn||NVO cell in its working state.

cantly superior to the cell without the NOPC protective layer that experiences rapid capacity degradation and fails after 1000 cycles (Fig. 5g). Besides, the button-type NOPC-Zn||NVO cell is capable of lighting up a blue LED strip (Fig. 5h), verifying its promising potential for practical applications.

In conclusion, a developed mesoporous NOPC material uniformly anchored with zincophilic nitrogen and oxygen sites, prepared by pyrolyzing ZIF-8 with NH_4Cl within its backbone, was used as a protective layer for enhancing the stability of Zn anode. The theoretical calculations and experimental studies demonstrate that the high-content N and O atoms in the NOPC layer serve as zincophilic nucleation sites, while the developed mesoporous structure homogenizes Zn^{2+} flux, enabling dendrite-free Zn deposition. The NOPC protective layer also effectively prevents interfacial side reactions like corrosion and HER, enhancing the reversibility of the Zn electrode. Consequently, the NOPC-Zn electrode exhibits outstanding stability with an ultra-long cycle life of over 6000 h in symmetric cells (1 mA/cm^2, 1 mAh/cm^2), and an impressive average CE of 99.8 % for 4600 cycles in asymmetric cells at 10 mA/cm^2. The NOPC-Zn||NVO full cell shows a capacity retention of 85.1 % after 3000 cycles. This work highlights the effectiveness of the carbon-based protective layer with both zincophilic heteroatom anchoring and developed meso–porosity in significantly improving the stability of Zn electrodes, providing a promising approach for the development of high-performance ZIBs.

CRediT authorship contribution statement

Zhuohua Li: Writing – original draft, Methodology, Investigation, Formal analysis, Conceptualization. **Qizhen Zhu:** Writing – review & editing, Supervision, Methodology, Conceptualization. **Yanze Li:** Investigation, Formal analysis, Data curation. **Yong Yang:** Investigation, Formal analysis. **Yuan Ju:** Investigation, Formal analysis. **Mengyao Xu:** Software, Investigation. **Bin Xu:** Writing – review & editing, Supervision, Software, Project administration, Methodology, Funding acquisition, Data curation, Conceptualization.

Declaration of competing interest

The authors declare that they have no known competing financial interests or personal relationships that could have appeared to influence the work reported in this paper.

Acknowledgment

The authors acknowledge the financial support by National Natural Science Foundation of China (No. U2004212).

Supplementary materials

Supplementary material associated with this article can be found, in the online version, at doi:10.1016/j.cclet.2025.111348.

References

[1] X. Guo, S. Zhang, H. Hong, et al., iScience 28 (2025) 111751.
[2] Z. Liu, R. Wang, Q. Ma, et al., Adv. Funct. Mater. 34 (2024) 2214538.
[3] R. Zhao, X. Dong, P. Liang, et al., Adv. Mater. 35 (2023) 2209288.
[4] Y. Geng, W. Xin, L. Zhang, et al., Natl. Sci. Rev. 12 (2025) nwae397.
[5] Z. Zhang, B. Xi, X. Ma, et al., SusMat 2 (2022) 114–141.
[6] P. Xue, C. Guo, W. Gong, et al., Angew. Chem. Int. Ed. 64 (2025) e202500295.
[7] Z. Zhang, P. Wang, C. Wei, et al., Angew. Chem. Int. Ed. 63 (2024) e202402069.
[8] J. Yang, P. Yang, W. Yan, et al., Energy Storage Mater. 51 (2022) 259–265.
[9] J. Zhou, F. Wu, Y. Mei, et al., Adv. Mater. 34 (2022) 2200782.
[10] N. Dong, X. Zhao, M. Yan, et al., Nano Energy 104 (2022) 107903.
[11] X. Cai, X. Wang, Z. Bie, et al., Adv. Mater. 36 (2024) 2306734.
[12] Y.F. Qu, J.W. Qian, F. Zhang, et al., Adv. Mater. 37 (2025) 2413370.
[13] H. Zhang, S. Li, L. Xu, et al., Adv. Energy Mater. 12 (2022) 2200665.
[14] W. Zhang, Q. Yao, C. Wang, et al., Adv. Funct. Mater. 34 (2024) 2303590.

[15] S. Chen, K. Ouyang, G. Pu, et al., Small 21 (2025) 2409654.
[16] Q. Wen, H. Fu, C. Sun, et al., Sci. Bull. 70 (2025) 518–528.
[17] Y. Song, Y. Liu, S. Luo, et al., Adv. Funct. Mater. 34 (2024) 2316070.
[18] G. Yoo, Y.R. Jo, G.H. An, ACS Energy Lett. 9 (2024) 5955–5965.
[19] D. Luo, B. Niu, P. Du, et al., Adv. Mater. 37 (2025) 2418741.
[20] H. Bian, C. Wang, Y. Wang, et al., Adv. Funct. Mater. 34 (2024) 2401760.
[21] Q. Yang, Y. Guo, B. Yan, et al., Adv. Mater. 32 (2020) e2001755.
[22] J. Wang, J. Peng, W. Huang, et al., Adv. Funct. Mater. 34 (2024) 2316083.
[23] S. Kim, G.H. Ryu, G.H. An, Appl. Surf. Sci. 635 (2023) 157634.
[24] W. Li, K. Wang, M. Zhou, et al., ACS Appl. Mater. Interfaces 10 (2018) 22059–22066.
[25] S.A. Haris, S. Adhami, R. Yuksel, et al., Small 21 (2025) 2501293.
[26] H. Du, R. Liang, X. Ji, et al., ACS Appl. Mater. Interfaces 16 (2024) 55502–55510.
[27] J. Zhou, M. Xie, F. Wu, et al., Adv. Mater. 33 (2021) 2101649.
[28] C. Wu, K. Xie, K. Ren, et al., Dalton Trans. 49 (2020) 17629–17634.
[29] W. Zheng, H. Xie, L. Zhu, et al., J. Energy Storage 76 (2024) 109808.
[30] Z. Sun, X. Jiao, S. Chu, et al., Chem. Eng. Sci. 298 (2024) 120358.
[31] H. Chen, N. Sun, Q. Zhu, et al., Adv. Sci. 9 (2022) 2200023.
[32] Q. Zhu, Q. Zhao, Y. An, et al., Nano Energy 33 (2017) 402–409.
[33] Z. Li, L. Feng, G. Huo, et al., ACS Appl. Nano Mater. 7 (2024) 3479–3487.
[34] N. Sun, R. Zhao, M. Xu, et al., J. Power Sources 564 (2023) 232879.
[35] F. Wan, L. Zhang, X. Dai, et al., Nat. Commun. 9 (2018) 1656.